

STRONG FIELD
DISSOCIATION AND
IONIZATION OF H_2^+



QUALIFYING EXAM

LUN YUE
20073474

SUPERVISOR: LARS BOJER MADSEN

JANUARY 2014

DEPARTMENT OF PHYSICS AND ASTRONOMY
GRADUATE SCHOOL OF SCIENCE AND TECHNOLOGY
AARHUS UNIVERSITY

Preface

This progress report contains a summary of some of the work done during part A of my Ph.D. studies at the Department of Physics and Astronomy, Aarhus University.

My project centers around ionization and dissociation processes in molecules exposed to intense laser pulses. Some time had been spent on the simulation of such processes using the theory of multi-configurational time-dependent Hartree-(Fock) theory, where it was realised that an efficient tool for extraction of observables was needed.

This report is centered around numerical studies of strong-field fragmentation of H_2^+ . An existing method has been extended to extract complete differential energy spectra of dissociation and dissociative ionization processes in H_2^+ . The extended method has been published in [1].

Notation

Atomic units $m_e = e = \hbar = 1$ are used throughout this report unless stated otherwise.

Acknowledgements

I would like to thank my supervisor Lars Bojer Madsen for excellent guidance throughout my studies.

Contents

Preface	i
Notation	i
Acknowledgements	i
Contents	ii
1 Introduction	1
2 H_2^+ in Laser Fields	3
2.1 The Hamiltonian operator	3
2.2 The 1D colinear model for H_2^+	4
2.3 Pure dissociation of H_2^+	4
2.4 The Keldysh parameter	5
3 Numerical Methods	6
3.1 The split-operator method	6
3.2 Complex absorbing potentials	8
3.3 Extraction of observables	8
4 Results and Discussion	15
4.1 Demonstration of the t-SURFF method	15
4.2 Frequency dependence of JES	19
4.3 Frequency dependence of JES - long wavelengths	24
4.4 Frequency dependence of JES - ultrashort pulse	24
5 Conclusion	26
5.1 Outlook	26
Bibliography	28

Chapter 1

Introduction

The interaction of atoms and molecules with radiation fields has been studied for several decades. With significant progress in laser technology during the past decades, ultrashort pulses with durations in the femtosecond (fs) time regime, and characterized by field strengths which are comparable to the Coulomb interaction between electrons and nuclei in atoms and molecules, are readily available. The interaction with atomic and molecular systems for pulses in this strong-field intensity range, usually $I = 10^{13} - 10^{15}$ W/cm², has prompted the discovery of a multitude of new strong-field phenomena. These phenomena include processes such as the above-threshold ionization (ATI) [2], where an atom or a molecule absorbs more photons than the minimum required to ionize; the above-threshold dissociation (ATD) [3, 4], where a molecule absorbs more photons than the minimum required to dissociate; above-threshold Coulomb explosion (ATCE) [5], where following the ionization of all electrons in a molecule the remaining bare nuclei dissociate with energies separated by the photon energies.

Another important process which needs mentioning is high-harmonic generation (HHG), where the non-linear interaction between laser and medium can be used to produce energetic photons with frequencies being a multiple of the laser frequency. The semi-classical three-step model [6] can be used to qualitatively understand this process: first, an electron is ionized into the continuum, where it is driven back and forth by the periodic field, continuously picking up energy from the field, then at a later time the electron can recombine with the parent ion with the excess energy being turned into the emission of a high energy photon. The process of HHG has many applications, one of which is the production of XUV sub-femtosecond laser pulses [7]. The achievement of producing pulses with femtosecond or subfemtosecond durations has sparked interest in measuring the dynamics of atoms and molecules on their natural time scales [7] and has led to entirely new research areas such as femtochemistry and attoscience. Typically, to obtain time-resolved information, pump-probe schemes have been used, where a pump pulse induces dynamics in the system under investigation and a subsequent probe pulse is applied after a fixed time-delay to extract time information [8, 9, 10, 11, 12].

All the above processes and schemes involve coupling to at least a single continuum, which from a theoretical and computational standpoint is challenging due to the requirement of an accurate description of the continua. This has led to the usage of different approximations in the description of ionization and dissociation in molecular systems, including the single-active electron approximation (SAE) where only a single electron couples to the field; the clamped nuclei approximation where the nuclei are assumed to be fixed in space; or the Born-Oppenheimer (BO) approximation where nuclear wave packets are treated as moving on electronic potential energy surfaces.

Thus, to completely understand the interplay between nuclear and electronic degrees of freedom, all degrees of freedom must be treated on the same footing. For this purpose, the simplest molecule, H_2^+ , is of special interest to physicists, since understanding the fundamental physical processes in this molecule will add valuable insight into more complex molecular systems. For the dissociative ionization (DI) process, the observable that can illustrate the electron-nuclei correlation effects during the interaction with a laser field is the joint energy spectrum (JES), which displays the differential probability for simultaneously detecting a particular electronic kinetic energy and a particular nuclear kinetic energy [13]. Recent numerical calculations [13, 14, 15] and experimental studies [16] have shown that rich electron-nuclei correlations indeed exist in strong field fragmentation.

In numerical solutions to the time-dependent Schrödinger equation (TDSE) in a finite simulation volume, extraction of continuum information such as the JES introduces an obstacle. One method is to wait until the bound and scattered part of the wavefunction are separated, whereafter a projection of the scattered part onto asymptotic channel eigenstates is performed [17, 18, 19]. This puts a lower limit on the size of the simulation volumes as the scattered part of the wavefunction must not reach the volume boundaries. Depending on field parameters, this usually requires a huge simulation volume, which is computationally challenging. Another method is to project the total wavefunction onto exact scattering states at the end of the time-dependent perturbation [20]. The advantage of this is that a somewhat smaller simulation volume can be used compared to the former method, while the drawback is the difficulty in obtaining the exact scattering states for a single continuum and the non-existence of exact scattering states for several continua.

The time-dependent surface flux (t-SURFF) method [21, 22] was recently introduced to extract fully differential ionization spectra of one and two-electron atomic systems from numerical TDSE calculations, using minimal simulation volumes. By placing absorbers at the grid boundaries that absorbed the outgoing electron flux, the total number of discretization points used was decreased, thereby reducing the numerical effort. Energy spectra are still obtainable by monitoring the flux passing through surfaces placed at distances smaller than the absorber regions. This method has been extended to treat dissociation and dissociative ionization of H_2^+ in [1].

This report centers around the dissociation and dissociative ionization of a simplified colinear model of the H_2^+ molecule when exposed to ultrashort pulses. Chapter 2 introduces the Hamiltonian and describes some general physical effects. In Chapter 3 the numerical method for solving the TDSE is sketched and the t-SURFF method for extraction of relevant observables is described. The demonstration of the methods and numerical results are presented and discussed in Chapter 4.

Chapter 2

H_2^+ in Laser Fields

2.1 The Hamiltonian operator

For a single-electron diatomic molecule with nuclear masses M_1 and M_2 and nuclear charges Z_1 and Z_2 interacting with a laser field, the Hamiltonian in the laboratory fixed frame with the electronic coordinate \vec{r}_e and the nuclear coordinates \vec{R}_1 and \vec{R}_2 can be written as

$$\begin{aligned}
 H_{\text{tot}}(t) = & -\frac{1}{2}\vec{\nabla}_{\vec{r}}^2 - \frac{1}{2M_1}\vec{\nabla}_{\vec{R}_1}^2 - \frac{1}{2M_2}\vec{\nabla}_{\vec{R}_2}^2 \\
 & + \frac{Z_1 Z_2}{|\vec{R}_1 - \vec{R}_2|} - \frac{Z_1}{|\vec{r}_e - \vec{R}_1|} - \frac{Z_2}{|\vec{r}_e - \vec{R}_2|} \\
 & + i\vec{A}(t) \left(-\vec{\nabla}_{\vec{r}_e} + \frac{Z_1}{M_1}\vec{\nabla}_{\vec{R}_1} + \frac{Z_2}{M_2}\vec{\nabla}_{\vec{R}_2} \right)
 \end{aligned} \tag{2.1}$$

It is convenient to transform using the Jacobi coordinates:

$$\begin{aligned}
 \vec{R}_{\text{CM}} &= \frac{M_1\vec{R}_1 + M_2\vec{R}_2 + \vec{r}_e}{M_1 + M_2 + 1} \\
 \vec{R} &= \vec{R}_1 - \vec{R}_2 \\
 \vec{r} &= \vec{r}_e - \frac{M_1\vec{R}_1 + M_2\vec{R}_2}{M_1 + M_2}
 \end{aligned} \tag{2.2}$$

where R_{CM} is the center of mass (CM) coordinate, \vec{R} is the relative coordinate of the two nuclei and \vec{r} is the electronic coordinate measured relative to the CM of the two nuclei. The Hamiltonian now takes on the form:

$$H_{\text{tot}}(t) = H_{\text{CM}}(t) + T_e + T_N + V_{eN} + V_N + V_I(t) \tag{2.3}$$

with

$$\begin{aligned}
 H_{\text{CM}} &= -\frac{1}{2(M_1 + M_2 + 1)}\vec{\nabla}_{\vec{R}_{\text{CM}}}^2 + i\alpha_{\text{CM}}\vec{A}(t)\vec{\nabla}_{\vec{R}_{\text{CM}}}, \\
 T_e &= -\frac{1}{2\mu}\vec{\nabla}_{\vec{r}}^2, \quad T_N = -\frac{1}{2M_N}\vec{\nabla}_{\vec{R}}^2, \\
 V_{eN} &= -\frac{Z_1}{|\vec{r} - \rho_1\vec{R}|} - \frac{Z_2}{|\vec{r} - \rho_2\vec{R}|}, \quad V_N = \frac{Z_1 Z_2}{R}, \\
 V_I(t) &= i\vec{A}(t) \left(\alpha_N\vec{\nabla}_{\vec{R}} - \beta\vec{\nabla}_{\vec{r}} \right)
 \end{aligned} \tag{2.4}$$

where

$$\begin{aligned} \mu &= \frac{M_1 + M_2}{M_1 + M_2 + 1}, & M_N &= \frac{M_1 M_2}{M_1 + M_2}, & \rho_1 &= \frac{M_2}{M_1 + M_2}, & \rho_2 &= \frac{M_1}{M_1 + M_2}, \\ \alpha_{\text{CM}} &= \frac{-1 + Z_1 + Z_2}{1 + M_1 + M_2}, & \alpha_N &= \frac{Z_1 M_2 - Z_2 M_1}{M_1 M_2}, & \beta &= \frac{M_1 + M_2 + Z_1 + Z_2}{M_1 + M_2} \end{aligned} \quad (2.5)$$

The CM motion can be separated out in the time dependent Schrödinger equation (TDSE) and solved exactly, with Volkov waves as solutions. The interesting Hamiltonian is the Hamiltonian for the relative motion:

$$H(t) = T_e + T_N + V_{eN} + V_N + V_I(t) \quad (2.6)$$

In this report the vector potential is assumed to be linearly polarized along the internuclear axis with a sine-squared envelope:

$$\vec{A}(t) = A_0 \sin^2 \left(\frac{\pi t}{T_{\text{pulse}}} \right) \cos(\omega t) \hat{R}, \quad (2.7)$$

where ω is the angular frequency and the pulse duration T_{pulse} is related to the number of optical cycles N_c by $T_{\text{pulse}} = N_c 2\pi/\omega$. The amplitude A_0 is chosen such that $\omega^2 A_0^2 = I$, with I denoting the peak intensity.

2.2 The 1D colinear model for H_2^+

For H_2^+ , which is a homo-nuclear molecule, the nuclear coordinate cannot couple to the field directly, as seen in Eq. (2.5) with $\alpha_N = 0$. The most important coordinate axis of the electron is the one along the polarization direction of the laser pulse, so a simplified model with reduced dimensionality of H_2^+ is employed that only includes the nuclear coordinate R and the electron coordinate x that is aligned with the pulse, shown in Fig. 2.1. Such models have been used extensively in the literature and reproduce experimental results at least qualitatively [23, 24, 25]. For our purposes, which is to investigate the nuclear and electron energy distributions, such a model is a good starting point. The Hamiltonian is still given by (2.6), now with

$$\begin{aligned} T_e &= -\frac{1}{2\mu} \frac{d^2}{dx^2}, & T_N &= -\frac{1}{m_p} \frac{d^2}{dR^2}, & V_I(t) &= -i\beta A(t) \frac{\partial}{\partial x} \\ V_{eN} &= -\frac{1}{\sqrt{(x - \frac{R}{2})^2 + a(R)}} - \frac{1}{\sqrt{(x + \frac{R}{2})^2 + a(R)}}, & V_N &= \frac{1}{R}, \end{aligned} \quad (2.8)$$

where $m_p = 1836$ is the proton mass and the softening parameter $a(R)$ for the Coulomb singularity is chosen to produce the exact three-dimensional $1s\sigma_g$ BO potential energy curve [13], so that the dynamics in this model is as close to the real three-dimensional case as possible.

2.3 Pure dissociation of H_2^+

If the dominant break-up process in H_2^+ is the dissociation process, the BO-approximation can be used for qualitative description of the dynamics. The adiabatic BO basis states

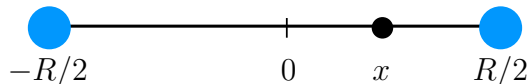


Figure 2.1: One dimensional colinear model of H_2^+ with electronic coordinate x and internuclear distance R , both along the polarization direction of the laser pulse.

$|\phi_{\text{el},i}\rangle$ can be obtained as the solutions to the electronic time-independent Schrödinger equation (TISE) with parametric dependence on R

$$\left(T_e + V_{\text{eN}} + V_{\text{N}}\right)|\phi_{\text{el},i}\rangle = E_{\text{el},i}(R)|\phi_{\text{el},i}\rangle, \quad (2.9)$$

where $E_{\text{el},i}(R)$ is the i 'th electronic potential energy surface in the BO approximation. To ease notation we do not explicitly include the parametric dependence on R in the BO-states.

Assume now that only the N lowest bound electronic states are involved in the dynamics. By making the ansatz $\Psi(x, R, t) = \sum_i^N G_i(R, t)\phi_{\text{el},i}(x, R)$ in the TDSE of Eq. (3.1), projecting on the BO basis states and neglecting term involving the first- and second-order derivatives of the electronic states with respect to R , the TDSE can be rewritten:

$$i\partial_t \vec{G}(R, t) = (\mathbf{H}^{(1)} + \mathbf{H}^{(2)}) \vec{G}(R, t) \quad (2.10)$$

where $\vec{G}(R, t) = [G_1(R, t), \dots, G_N(R, t)]^T$, $\mathbf{H}^{(1)}$ is a diagonal $N \times N$ matrix with matrix elements $H_{ij}^{(1)} = \left[-\frac{1}{m_p} \frac{\partial^2}{\partial R^2} + E_{\text{el},i}(R)\right] \delta_{i,j}$ and $\mathbf{H}^{(2)}$ is a $N \times N$ off-diagonal matrix containing the electron-field coupling. Due to the neglect of some of the excited and continuum electronic states in the ansatz, the dynamics are only correctly described in the length gauge [26], so that $H_{ij}^{(2)}(t) = \beta_{\text{LG}} \langle \phi_{\text{el},i}(R) | x | \phi_{\text{el},j}(R) \rangle F(t)$, with the electric field $F(t) = -\partial_t A(t)$ and $\beta_{\text{LG}} = 1 + 1/(2m_p + 1)$. We will refer to this model as the N -surface model. In this report, N -surface model with $N = 2, 4, 6$ will be investigated.

2.4 The Keldysh parameter

The Keldysh parameter γ , first introduced by Keldysh in 1964 [27], is given by:

$$\gamma = \sqrt{\frac{I_p}{2U_p}} = \frac{\omega \sqrt{2I_p}}{F_0} \quad (2.11)$$

where I_p is the ionization potential, $F_0 = \omega A_0$ is the peak electric field strength and $U_p = A_0^2/4$ the ponderomotive potential corresponding to the cycle-averaged kinetic energy of a classical electron in a sinusoidal electric field oscillating at angular frequency ω . The Keldysh parameter gives an rough estimate of the adiabaticity of the photo-ionization process, and it can be interpreted as the ratio between the characteristic time it takes for the electron to tunnel through the distorted barrier formed by the electric field and the static Coulomb potential, and the characteristic time of the laser oscillation. In the regime of high-intensity and low-frequency fields, $\gamma \ll 1$, the electron would have sufficient time to tunnel through the barrier and the ionization is said to occur in the tunnel-ionization regime. For fields with low intensity and high frequency, the field changes sign so quickly that the electron has no time to tunnel and ionization is said to be happening in the multi-photon regime.

Chapter 3

Numerical Methods

This chapter introduces the numerical methods used for the propagation and extraction of observables for the one-dimensional H_2^+ model interacting with an intense laser pulse.

3.1 The split-operator method

The method used for propagation is the split-operator, fast Fourier transform (FFT) method [28]. Consider the TDSE for the colinear 1D model H_2^+ interacting with a laser pulse

$$i\partial_t|\Psi(t)\rangle = H(t)|\Psi(t)\rangle, \quad (3.1)$$

with the Hamiltonian given by (2.6) and (2.8):

$$H(t) = T_e + T_N + V_{eN} + V_N + V_I(t). \quad (3.2)$$

If the wave function Ψ is known at time t , the short time propagator $U(t + \Delta t, t)$ used to obtain the wave function at a later time $t + \Delta t$ can be written:

$$U(t + \Delta t, t) = e^{-i\frac{\Delta t}{2}(T_e + T_N + V_I(t))} e^{-i\Delta t(V_{eN} + V_N)} e^{-i\frac{\Delta t}{2}(T_e + T_N + V_I(t))} + O(\Delta t^3), \quad (3.3)$$

where $O(\Delta t^3)$ denotes error terms proportional to third and higher orders in Δt . By chosen a time-step Δt that is much smaller than the characteristic time-scale of the Hamiltonian, the error terms can be neglected. In this report a time-step of $\Delta t = 0.005$ is used.

The propagation scheme is performed by consecutively representing the wavefunction in a basis that diagonalizes the operator in question. The $V_{eN} + V_N$ is diagonal in coordinate representation, while $T_e + T_N + V_I$ is diagonal in momentum representation. Let p now denote the electronic momentum and k the nuclear momentum. We proceed by defining equidistant grid points in the two representations with N_e grid points for the electronic degree of freedom and N_N grid points for the nuclear degree of freedom:

$$\begin{aligned} x_l &= x_0 + l\Delta x, & p_m &= p_0 + m\Delta p, & (l, m &= 1, \dots, N_e - 1) \\ R_j &= R_0 + j\Delta R, & k_n &= k_0 + n\Delta k, & (j, n &= 1, \dots, N_N - 1) \end{aligned} \quad (3.4)$$

where L_e and L_N are the length of the electronic and nuclear coordinate grids, respectively, and $\Delta x = L_e/N_e$, $\Delta R = L_N/N_N$, $\Delta p = 2\pi/L_e$, $\Delta k = 2\pi/L_N$. The wavefunction in coordinate representation Ψ can be written in terms of the backward Fourier transform

(FT) of the momentum wave function Φ :

$$\Psi(x_l, R_j, t) = \frac{\Delta p \Delta k}{2\pi} \sum_m^{N_e} \sum_n^{N_N} \Phi(p_m, k_n, t) e^{ip_m x_l} e^{ik_n R_j} \quad (3.5)$$

with the momentum wave function given as the forward FT of the wave function in coordinate representation:

$$\Phi(p_m, k_n, t) = \frac{\Delta x \Delta R}{2\pi} \sum_l^{N_e} \sum_j^{N_N} \Psi(x_l, R_j, t) e^{-ip_m x_l} e^{-ik_n R_j} \quad (3.6)$$

During each step of the time-propagation, the following steps must be carried out:

- (a) Forward FT the wave function from position space into momentum space

$$\Psi(x_l, R_j, t) \xrightarrow{\text{forward FT}} \Phi(p_m, k_n, t) \quad (3.7)$$

and apply the first factor in the short-time propagator (3.3)

$$\Phi(p_m, k_n, t) \rightarrow \Phi^{(1)}(p_m, k_n, t) \equiv e^{-i\frac{\Delta t}{2} \left(\frac{p_m^2}{2\mu} + \frac{k_n^2}{m_p} + \beta A(t) p_m \right)} \Phi(p_m, k_n, t) \quad (3.8)$$

- (b) Backward FT into position space

$$\Phi^{(1)}(p_m, k_n, t) \xrightarrow{\text{backward FT}} \Psi^{(1)}(x_l, R_j, t) \quad (3.9)$$

and apply the second factor in the short-time propagator (3.3) involving the time-independent potential terms

$$\Psi^{(1)}(x_l, R_j, t) \rightarrow \Psi^{(2)}(x_l, R_j, t) \equiv e^{-i\Delta t (V_{eN}(x_l, R_j) + V_N(R_j))} \Psi^{(1)}(x_l, R_j, t) \quad (3.10)$$

- (c) Forward FT into position space

$$\Psi^{(2)}(x_l, R_j, t) \xrightarrow{\text{forward FT}} \Phi^{(2)}(p_m, k_n, t) \quad (3.11)$$

and apply the last factor in the short-time propagator (3.3)

$$\Phi^{(2)}(p_m, k_n, t) \rightarrow \Phi^{(3)}(p_m, k_n, t) \equiv e^{-i\frac{\Delta t}{2} \left(\frac{p_m^2}{2\mu} + \frac{k_n^2}{m_p} + \beta A(t) p_m \right)} \Phi^{(2)}(p_m, k_n, t) \quad (3.12)$$

- (d) Complete the short-time propagation by backward FT into position space to obtain the wave function at time $t + \Delta t$

$$\Phi^{(3)}(p_m, k_n, t) \xrightarrow{\text{backward FT}} \Psi(x_l, R_j, t + \Delta t). \quad (3.13)$$

In the above scheme, most of computational effort will occur in the two-dimensional discrete FT that has to be performed multiple times at each time step. With the Cooley-Tukey fast fourier transformation (FFT) algorithm the scaling of each transform with respect to the number of gridpoints is in the order of $N_e N_N \log(N_e N_N)$, which is manageable on modern-day computers for reasonable choices of N_N and N_N .

For the N -surface model described in Sec. 2.3, a split-operator, FFT scheme is also used for the time-propagation. Here, the $N \times N$ off-diagonal matrix $\mathbf{H}^{(2)}$ in (2.10) has to be diagonalized for all internuclear distances R and stored in memory. Most computational effort is now in the N one-dimensional FFTs that has to be performed, which scales as $NN_N \log(N_N)$. As expected, the N -surface model is seen to be much faster than the full TDSE calculation where x and R are treated on the same footing.

3.2 Complex absorbing potentials

When a molecule interacts with a strong laser pulse, it can ionize and dissociate. The ionized and the dissociative wave packets can travel great distances during the duration of the pulse length, and if this distance is greater than the grid sizes, unphysical reflections can occur at the grid boundaries. To extract correct observables it is therefore crucial to make sure that the wave packets do not reach the boundary of the simulation volume. One method to achieve this is the usage of a complex absorbing potential (CAP) [29] near the box boundaries that can absorb the outgoing wavepackets without modifying the physical wavefunction in the inner part of the grid.

Consider a monomial CAP on the form:

$$V_{\text{CAP}}(x, R) = \begin{cases} -i\eta_e (|x| - x_{\text{CAP}})^{n_e} - i\eta_N (R - R_{\text{CAP}})^{n_N}, & |x| > x_{\text{CAP}}, R > R_{\text{CAP}} \\ 0, & \text{elsewhere} \end{cases} \quad (3.14)$$

If acted on the wave function at time t during the split-operator propagation, the effect is to reduce the amplitude of the wave packet inside the CAP region:

$$e^{-iV_{\text{CAP}}(x,R)}\Psi(x, R, t) = e^{-\eta_e(|x|-x_{\text{CAP}})^{n_e}} e^{-\eta_N(R-R_{\text{CAP}})^{n_N}} \Psi(x, R, t). \quad (3.15)$$

The CAP, being a numerical artifact imposed on the physical system, is not a perfect absorber and will always cause some reflections. For the calculations in this report the parameter values $\eta_e = 0.001$, $x_{\text{CAP}} = 110$, $n_e = 2$, $\eta_N = 0.01$, $R_{\text{CAP}} = 26$ and $n_N = 2$ were used, which were numerically tested to cause minimal reflections for the problems considered in this report.

3.3 Extraction of observables

As mentioned in the introduction of Chapter 1, the t-SURFF method [21, 22] was introduced to extract fully differential ionization spectra of one and two-electron atomic systems from numerical TDSE calculations. The extension of this method to treat for dissociation and DI in the H_2^+ molecule is described in following.

t-SURFF for H_2^+ - partition of coordinate space

The basic idea of the method is to monitor the flux passing through surfaces placed at distances smaller than the absorber regions, and afterwards construct the relevant differential distributions. For H_2^+ interacting with a laser pulse, there are two continuum channels:

- The DI channel $\text{H}_2^+ \rightarrow \text{p} + \text{p} + \text{e}$, where the final asymptotic state consists of two protons and one electron separated by large distances. The observable of interest is the JES that shows the energy sharing between the protons and the electron. From the JES, the electronic above threshold ionization (ATI) and the nuclear KER spectra are obtained by integrating out the appropriate degrees of freedom.
- The dissociation channel $\text{H}_2^+ \rightarrow \text{H} + \text{p}$, where H_2^+ dissociates into a proton and a hydrogen atom in a given state (channel). The relevant observables are

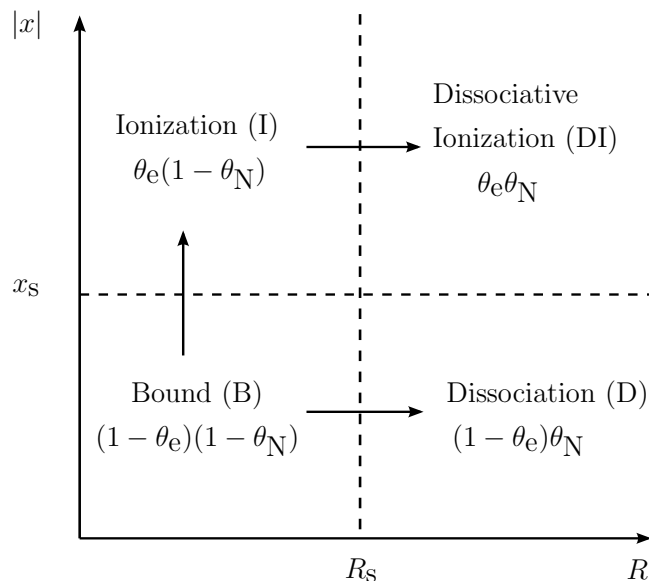


Figure 3.1: Illustration showing the four spatial regions used to analyse the wave packet formed by the interaction of H_2^+ with the external laser pulse. The dashed line at $|x| = x_s$ is a boundary surface beyond which the electron-nuclear interaction V_{eN} is neglected in the DI channel, while the dashed line at $R = R_s$ is a boundary surface beyond which the nuclear repulsion V_N is neglected. In the t-SURFF method, the flux passing through these surfaces is monitored and used to construct the differential probability amplitudes. In the figure, the projection operators, formed from Eqs. (3.16a) and (3.16b), that project on the different spatial regions are given in the corresponding reaction channels.

the channel specific KER spectra that show how the nuclear kinetic energies are shared between the different dissociation channels.

To identify the different channels and the corresponding observables, we partition the total coordinate space into four regions as shown in Fig. 3.1. Each region corresponds to a reaction channel. By monitoring the flux going through the surfaces at $|x| = x_s$ and $R = R_s$, the JES for DI and the channel-specific KER for dissociation can be constructed.

To proceed formally, we define the projection operators

$$\theta_e = \int dx \theta(|x| - x_s) |x\rangle \langle x|, \quad (3.16a)$$

$$\theta_N = \int dR \theta(R - R_s) |R\rangle \langle R|, \quad (3.16b)$$

where x_s and R_s are locations of the surfaces beyond which the Coulomb interactions V_{eN} and V_N can be neglected, respectively, and $\theta(x)$ is the Heaviside step function. These projection operators are used to partition the total wavefunction into the four parts belonging to the different spatial regions of Fig. 3.1,

$$|\Psi(t)\rangle = |\Psi_B(t)\rangle + |\Psi_D(t)\rangle + |\Psi_I(t)\rangle + |\Psi_{DI}(t)\rangle, \quad (3.17)$$

with $|\Psi_B(t)\rangle = (1 - \theta_e)(1 - \theta_N)|\Psi(t)\rangle$, $|\Psi_D(t)\rangle = (1 - \theta_e)\theta_N|\Psi(t)\rangle$, $|\Psi_I(t)\rangle = \theta_e(1 - \theta_N)|\Psi(t)\rangle$, and $|\Psi_{DI}(t)\rangle = \theta_e\theta_N|\Psi(t)\rangle$. For sufficiently large times after the end of

the laser pulse $T > T_{\text{pulse}}$, the dissociation and DI wave packets will have moved into their specific spatial regions such that $|\Psi_{\text{B}}(T)\rangle$ contains the bound part of the total wave packet, $|\Psi_{\text{D}}(T)\rangle$ contains the dissociative part, and $|\Psi_{\text{DI}}(T)\rangle$ contains the DI part. At time T , the wave packet in the spatial region corresponding to ionization $|\Psi_{\text{I}}(T)\rangle = \theta_{\text{e}}(1 - \theta_{\text{N}})|\Psi(T)\rangle = 0$, as all the ionized part will have moved into the DI region since the nuclei do not support bound states after the removal of the electron.

t-SURFF for dissociative ionization

With the partitioning of space and wave functions, we are now ready to consider the formulation of the t-SURFF methodology for the DI channel $\text{H}_2^+ \rightarrow \text{p} + \text{p} + \text{e}$. The projected TDSE on the spatial region describing this channel reads (see Fig. 3.1)

$$i\partial_t|\Psi_{\text{DI}}(t)\rangle = H_{\text{DI}}(t)|\Psi(t)\rangle, \quad (3.18)$$

where we have defined the projected Hamiltonian $H_{\text{DI}}(t) = \theta_{\text{e}}\theta_{\text{N}}H(t) = T_{\text{e}} + T_{\text{N}} + V_{\text{I}}(t)$. It is important to notice that $|\Psi(t)\rangle$, not $|\Psi_{\text{DI}}(t)\rangle$, appears on the right-hand-side of Eq. (3.18). This reflects that $H(t)$ does not commute with $\theta_{\text{e}}\theta_{\text{N}}$ for all times t .

The TDSE for $H_{\text{DI}}(t)$ is separable in the electronic and nuclear degrees of freedom, with the electronic TDSE given by

$$i\partial_t|\phi(t)\rangle = (T_{\text{e}} + V_{\text{I}}(t))|\phi(t)\rangle, \quad (3.19)$$

and the nuclear TDSE given by

$$i\partial_t|\chi(t)\rangle = T_{\text{N}}|\chi(t)\rangle. \quad (3.20)$$

A complete set of the solutions in position space is formed by the Volkov waves $\phi_p(x, t) = \langle x|\phi_p(t)\rangle$ with momentum p for the electronic degree of freedom and plane waves $\chi_k(R, t) = \langle R|\chi_k(t)\rangle$ with momentum k for the nuclear degree of freedom. The explicit forms of these wave functions, with normalizations $\delta(k - k') = \langle \chi_k(t)|\chi_{k'}(t)\rangle$ and $\delta(p - p') = \langle \phi_p(t)|\phi_{p'}(t)\rangle$, are

$$\phi_p(x, t) = (2\pi)^{-1/2} \exp \left[i \left(px - \frac{p^2 t}{2\mu} - \frac{p}{\mu} \int^t A(t') dt' \right) \right], \quad (3.21)$$

$$\chi_k(R, t) = (2\pi)^{-1/2} \exp \left[i \left(kR - \frac{k^2 t}{m_{\text{p}}} \right) \right]. \quad (3.22)$$

The wave packet $|\Psi_{\text{DI}}(t)\rangle$ is expanded in the direct product basis of Volkov and plane waves

$$|\Psi_{\text{DI}}(t)\rangle = \theta_{\text{e}}\theta_{\text{N}}|\Psi(t)\rangle = \int dp \int dk b_{p,k}(t) |\phi_p(t)\rangle |\chi_k(t)\rangle, \quad (3.23)$$

where

$$b_{p,k}(T) = \langle \phi_p(t) | \langle \chi_k(t) | \theta_{\text{e}}\theta_{\text{N}} | \Psi(t) \rangle \quad (3.24)$$

is the differential probability amplitude for measuring an electronic momentum p and a nuclear momentum k . The joint momentum spectrum (JMS) reads

$$\frac{\partial^2 P}{\partial p \partial k} = |b_{p,k}(T)|^2. \quad (3.25)$$

The corresponding JES that gives the differential probability for observing a nuclear KER of $E_N = k^2/m_p$ and an electron with energy $E_e = p^2/2\mu$ is given by

$$\frac{\partial^2 P}{\partial E_e \partial E_N} = \sum_{\text{sgn}(p)} \frac{m_p \mu}{2|p|k} |b_{p,k}(T)|^2, \quad (3.26)$$

where the summation over $\text{sgn}(p)$ refers to the summation of $\pm p$ corresponding to the same E_e .

The expression for $b_{p,k}(T)$ is rewritten using Eqs. (3.18)-(3.20) and the fundamental theorem of analysis. The result reads

$$b_{p,k}(T) = b_{p,k}^e(T) + b_{p,k}^N(T) \quad (3.27)$$

with

$$b_{p,k}^e(T) = i \int_{-\infty}^T dt \langle \phi_p(t) | [T_e + V_I(t), \theta_e] \langle \chi_k(t) | \theta_N | \Psi(t) \rangle, \quad (3.28)$$

and

$$b_{p,k}^N(T) = i \int_{-\infty}^T dt \langle \chi_k(t) | [T_N, \theta_N] \langle \phi_p(t) | \theta_e | \Psi(t) \rangle. \quad (3.29)$$

In Eqs. (3.28) and (3.29), the commutators vanish everywhere except at the discontinuity of the step functions. The probability amplitudes can thus be obtained by integrating the time-dependent surface flux. The amplitude $b_{p,k}^e(T)$ is the amplitude corresponding to the flux going from the dissociation region into the DI region (see Fig. 3.1), while $b_{p,k}^N(T)$ is the amplitude corresponding to the flux going from the ionization region into the DI region. The two amplitudes must be added coherently to obtain the total amplitude for DI. It is, however, possible to choose R_s sufficiently large so that all the flux going into the DI region in Fig. 3.1 originate from the ionization region, and therefore we can set $b_{p,k}^e(T) = 0$. The commutators in Eqs. (3.28) and (3.29) can be calculated explicitly, with

$$[T_e + V_I(t), \theta_N] = \int dx |x\rangle \left[-\frac{1}{2\mu} \delta^{(1)}(|x| - x_s) - \text{sgn}(x) \delta(|x| - x_s) \left(\frac{1}{\mu} \frac{\partial}{\partial x} + i\beta A(t) \right) \right] \langle x|, \quad (3.30)$$

and

$$[T_N, \theta_N] = -\frac{1}{m_p} \int dR |R\rangle \left[\delta^{(1)}(R - R_s) + 2\delta(R - R_s) \frac{\partial}{\partial R} \right] \langle R|, \quad (3.31)$$

where δ and $\delta^{(1)}$ are the Dirac delta function and its first derivative, respectively. After inserting Eq. (3.31) into Eq. (3.29), evaluating the resulting integral and collecting terms in Eq. (3.27), we obtain

$$b_{p,k}(T) = \frac{1}{m_p} \int_{-\infty}^T dt \chi_k^*(R_s, t) \left[k - i \frac{\partial}{\partial R} \right] \langle \phi_p(t) | \theta_e | \Psi(t) \rangle \Big|_{R_s}. \quad (3.32)$$

To calculate the amplitude of Eq. (3.32), the matrix element $\langle \phi_p(t) | \theta_e | \Psi(t) \rangle$ must be evaluated at R_s . Direct projection of $\theta_e | \Psi(t) \rangle$ on the Volkov waves $|\chi_p(t)\rangle$ is not an option as the electronic CAP [Eq. (3.15)] will absorb part of the wavefunction at $|x| > x_{\text{CAP}} > x_s$. To circumvent this problem we expand $\langle \phi_p(t) | \theta_e | \Psi(t) \rangle$ in an arbitrary time-independent basis $\zeta_m(R)$

$$\langle \phi_p(t) | \theta_e | \Psi(t) \rangle = \sum_m a_{p,m}(t) | \zeta_m \rangle \quad (3.33)$$

with $a_{p,m}(t) = \langle \zeta_m | \langle \phi_p(t) | \theta_e | \Psi(t) \rangle$. In our calculations we use a sine basis for ζ_m . By taking the time derivative of $a_{p,m}(t)$ and using Eq. (3.30) to evaluate the resulting commutator, it can be shown that $a_{p,m}(t)$ satisfies

$$\frac{d}{dt} a_{p,m}(t) = -i \sum_{m'} \langle \zeta_m | T_N + V_N | \zeta_{m'} \rangle a_{p,m'}(t) + f_{p,m}^+(t) + f_{p,m}^-(t) \quad (3.34)$$

with

$$f_{p,m}^+(t) = \phi_p^*(x_s, t) \left[\left(\frac{p}{2\mu} + \beta A(t) \right) - \frac{i}{2\mu} \frac{\partial}{\partial x} \right] \langle \zeta_m | \Psi(t) \rangle \Big|_{x_s} \quad (3.35)$$

and

$$f_{p,m}^-(t) = -\phi_p^*(-x_s, t) \left[\left(\frac{p}{2\mu} + \beta A(t) \right) - \frac{i}{2\mu} \frac{\partial}{\partial x} \right] \langle \zeta_m | \Psi(t) \rangle \Big|_{-x_s}. \quad (3.36)$$

The terms $f_{p,m}^+(t)$ and $f_{p,m}^-(t)$ can be interpreted as flux terms, counting the flux going through the surfaces at $x = x_s$ and at $x = -x_s$, respectively. Equation (3.34) can be solved using any of the standard numerical techniques for solving ordinary differential equations; in our calculations we use a fourth-order Runge-Kutta method with time-step 0.05. The coefficients $a_{p,m}(t)$ give us information on the wave packet even in regions where the CAP is active ($|x| > x_{\text{CAP}} > x_s$), as seen in Eq. (3.33). When describing laser ionization, one of the two terms in $f_{p,m}(t)$ will usually be negligible and can therefore be ignored. For example if p is positive, then f^- will be zero since in this case there is no incoming wave at $x = -x_s$.

Inserting Eq. (3.33) into Eq. (3.32), we obtain the final expression for $b_{p,k}(T)$ determining the JMS and JES through Eqs. (3.25) and (3.26)

$$b_{p,k}(T) = \frac{1}{m_p} \sum_m \left[k - i \frac{\partial}{\partial R} \right] \zeta_m(R) \Big|_{R_s} \int_{-\infty}^T dt \chi_k^*(R_s, t) a_{p,m}(t). \quad (3.37)$$

t-SURFF for dissociation

Consider now the dissociation process $\text{H}_2^+ \rightarrow \text{H} + \text{p}$. The projected TDSE on the region describing dissociation without ionization reads (see Fig. 3.1)

$$i \partial_t | \Psi_D(t) \rangle = H_D(t) | \Psi(t) \rangle, \quad (3.38)$$

where we have defined the projected Hamiltonian $H_D(t) = (1 - \theta_e) \theta_N H(t)$. On the right-hand-side $| \Psi(t) \rangle$ and not $| \Psi_D(t) \rangle$ appears [see Eq. (3.18)].

To obtain the dissociation-channel-specific nuclear KER spectrum, we first expanded the wave packet $\Psi_D(x, R, t)$ in the BO basis $| \phi_{\text{el},i} \rangle$ of (2.9):

$$\begin{aligned} | \Psi_D(t) \rangle &= (1 - \theta_e) \theta_N | \Psi(t) \rangle \\ &= \int dk \sum_i c_{i,k}(t) | \chi_k(t) \rangle | \phi_{\text{el},i}(t) \rangle, \end{aligned} \quad (3.39)$$

where $| \chi_k(t) \rangle$ is a plane wave with momentum k given in Eq. (3.22), $| \phi_{\text{el},i}(t) \rangle = | \phi_{\text{el},i} \rangle e^{-iE_{\text{el},i}(R)t}$ and

$$c_{i,k}(t) = \langle \chi_k(t) | \langle \phi_{\text{el},i}(t) | (1 - \theta_e) \theta_N | \Psi(t) \rangle. \quad (3.40)$$

The bracket notation used here indicates integration with respect to both the electronic and nuclear degrees of freedom.

In Eq. (3.39), all the trivial time-dependence is included in $|\phi_{\text{el},i}(t)\rangle$ and $|\chi_k(t)\rangle$, while the non-trivial time dependence due to the external field and flux going from the bound region into the dissociation region of Fig. 3.1 is included in the expansion coefficients $c_{i,k}(t)$. At time $T > T_{\text{pulse}}$, when all the dissociative parts of the wave packet have moved into the dissociative region, $c_{i,k}(T)$ describes the differential probability amplitude for the electron to be in the bound state i and the nuclear degree of freedom to have momentum k .

The expression for $c_{i,k}(T)$ can be written as:

$$c_{i,k}(T) = c_{i,k}^{\text{N}}(T) + c_{i,k}^{\text{e}}(T) + c_{i,k}^{\text{I}}(T), \quad (3.41)$$

with

$$c_{i,k}^{\text{N}}(T) = i \int_{-\infty}^T dt \langle \chi_k(t) | [T_{\text{N}}, \theta_{\text{N}}] \langle \phi_{\text{el},i}(t) | (1 - \theta_{\text{e}}) | \Psi(t) \rangle, \quad (3.42)$$

$$c_{i,k}^{\text{e}}(T) = i \int_{-\infty}^T dt \langle \phi_{\text{el},i}(t) | [T_{\text{e}} + V_{\text{eN}} + V_{\text{N}}, (1 - \theta_{\text{e}})] \langle \chi_k(t) | \theta_{\text{N}} | \Psi(t) \rangle, \quad (3.43)$$

$$c_{i,k}^{\text{I}}(T) = -i \int_{-\infty}^T dt \langle \phi_{\text{el},i}(t) | \langle \chi_k(t) | (1 - \theta_{\text{e}}) \theta_{\text{N}} V_{\text{I}}(t) | \Psi(t) \rangle. \quad (3.44)$$

In the derivation of Eq. (3.42), it is assumed that the action of the nuclear kinetic energy operator on the electronic BO-states can be neglected. This is in accordance with the BO approximation wherein the first- and second-order derivatives of the electronic state with respect to R are neglected.

In Fig. 3.1, The amplitude $c_{i,k}^{\text{N}}(T)$ corresponds to the flux going from the bound region into the dissociation region through the surface at $R = R_{\text{s}}$, while $c_{i,k}^{\text{e}}(T)$ corresponds to the flux going through the surfaces at $x = \pm x_{\text{s}}$. The amplitude $c_{i,k}^{\text{e}}$ can thus be neglected if the dissociative wave packet never reaches the surface $x = \pm x_{\text{s}}$ at time T . In the pure dissociation process, the electron is localized near one of the protons, i.e., along the lines $x = \pm(1/2)R$. The previous condition can thus always be satisfied if we choose $x_{\text{s}} > R_{\text{s}}/2$.

The amplitude $c_{i,k}^{\text{I}}(T)$ in Eq. (3.44) includes the time-dependent interaction $V_{\text{I}}(t)$. Let T_{impact} be the instant at which the fastest part of the dissociative wave packet hits the surface $R = R_{\text{s}}$. Then $c_{i,k}^{\text{I}}(T)$ can be neglected as long as $T_{\text{impact}} \geq T_{\text{pulse}}$. This can be seen by rewriting Eq. (3.44) as

$$c_{i,k}^{\text{I}}(T) = -i \int_{-\infty}^T dt \left\{ \langle \phi_{\text{el},i}(t) | \langle \chi_k(t) | V_{\text{I}}(t) (1 - \theta_{\text{e}}) \theta_{\text{N}} | \Psi(t) \rangle + \langle \phi_{\text{el},i}(t) | \langle \chi_k(t) | \left[(1 - \theta_{\text{e}}), V_{\text{I}}(t) \right] \theta_{\text{N}} | \Psi(t) \rangle \right\} \quad (3.45)$$

with the commutator in the velocity gauge given by

$$\left[(1 - \theta_{\text{e}}), V_{\text{I}}(t) \right] = -i\beta A(t) \int dx |x\rangle \text{sgn}(x) \delta(|x| - x_{\text{s}}) \langle x|. \quad (3.46)$$

For $T_{\text{impact}} \geq T_{\text{pulse}}$, both terms in Eq. (3.45) are zero. The first term is zero because $|\Psi_{\text{D}}(t)\rangle = (1 - \theta_{\text{e}}) \theta_{\text{N}} |\Psi(t)\rangle = 0$ for $t < T_{\text{pulse}}$, while $V_{\text{I}}(t) = 0$ for $t > T_{\text{pulse}}$. Similarly,

the second term is zero because $\Psi(\pm x_s, R, t) = 0$. The condition $T_{\text{impact}} \geq T_{\text{pulse}}$ depends on the interaction $V_I(t)$ and can be satisfied by placing the R_s appropriately.

The final expression for $c_{i,k}(T)$ is then, using Eqs. (3.31) and (3.41),

$$c_{i,k}(T) = \frac{1}{m_p} \int_{-\infty}^T dt \chi_k^*(R_s, t) \left[k - i \frac{\partial}{\partial R} \right] \langle \phi_{\text{el},i}(t) | (1 - \theta_e) | \Psi(t) \rangle \Big|_{R_s}. \quad (3.47)$$

We see that the differential probability amplitude $c_{i,k}(T)$ can be calculated by monitoring the flux going through the surface $R = R_s$. Moreover, the electronic BO-states $\phi_{\text{el},i}(x; R)$ with parametric dependence on R only has to be calculated at points close to R_s , reducing the numerical effort.

The BO-states $|\phi_{\text{el},i}\rangle$, $i = 0, 1, \dots$ are even for i even, and odd for i odd. For sufficiently large R , the states become pairwise degenerate. It is therefore natural to order the states into pairs, each pair consisting of a gerade and an ungerade state, $\phi_{\text{el},i}^s$, $i = 0, 1, \dots$, with $s = g, u$. In the dissociation process, the differential probability for the nuclei to have a nuclear KER E_N and the electron to be in the i 'th electronic state with parity s is therefore given by

$$\frac{\partial P_i^s}{\partial E_N} = \frac{m_p}{2k} |c_{i,k}^s|^2, \quad (3.48)$$

where the amplitude $c_{i,k}^s$ is given in Eq. (3.47).

t-SURFF for dissociation - N -surface model

The KER spectrum in the N -surface model can also be obtained by the t-SURFF method. The dissociation-channel-specific differential probability amplitudes $c_{i,k}^{N-\text{BO}}(T)$, with $i = 0, \dots, N - 1$, corresponding to the N BO states, read

$$\begin{aligned} c_{i,k}^{N-\text{BO}}(T) &= \langle \chi_k(T) | \theta_N | G_i(T) \rangle \\ &= \frac{1}{m_p} \int_{-\infty}^T dt \chi_k^*(R_s, t) \left[k - i \frac{\partial}{\partial R} \right] G_i(t) \Big|_{R_s}, \end{aligned} \quad (3.49)$$

which is obtained using the techniques of the previous two subsections. As in the previous subsection, we have assumed that the laser pulse is over at the time the dissociative wave packet first hits the surface R_s . To check this method, the dissociative spectrum within the 2-surface model obtained using t-SURFF was compared with the results in Ref. [3] and a perfect match was observed.

Chapter 4

Results and Discussion

In this chapter we first demonstrate that the t-SURFF method indeed can treat, on an equal footing, dissociation and dissociative ionization of H_2^+ in intense laser fields. Subsequently, the JES for laser pulses with parameters ranging from the multi-photon regime to the tunneling regime are investigated.

4.1 Demonstration of the t-SURFF method

To demonstrate the t-SURFF method for H_2^+ , the laser pulse is applied with H_2^+ initially in the ground state. The ground state is obtained by propagation in imaginary time. The laser pulse parameters are $\lambda = 400$ nm, $N_c = 10$, and $I = 8.8 \times 10^{13}$ W/cm². The pulse duration is $T_{\text{pulse}} = 13.3$ fs, the photon energy is $\omega = 3.1$ eV and the Keldysh parameter [27] is $\gamma = 3.4$, indicating that the dynamics take place in the multiphoton ionization regime. These pulse parameters are chosen to facilitate comparisons with recent calculations using the same model for H_2^+ [13, 30]. All the following results are obtained with $x_s = 100$ and $R_s = 25$. Convergence of all results are checked by performing calculations with varying grid spacings, simulation volumes, CAP parameters, placement of t-SURFF surfaces, and observing that the results match. The time T , at which the dissociation and DI wave packets have moved inside their respective regions (see Fig. 3.1), is written as $T = T_{\text{pulse}} + T_{\text{free}}$, with T_{free} being the propagation time after the pulse. An estimate of T_{free} for DI can be made by assuming the slowest nuclei to have $E_N = 1/R_{\text{cl},0}$, where $R_{\text{cl},0}$ is the outer classical turning point of the ground vibrational state. An estimate for T_{free} is then given by $R_s \sqrt{R_{\text{cl},0} m_p / 2} = 932$. To obtain a more accurate T_{free} numerical tests are performed, and it is found that choosing $T_{\text{free}} = 1200$ will lead to the convergence of both the dissociation and the DI spectra.

Figure 4.1 shows the JES spectrum for the DI process of H_2^+ with the above-mentioned laser parameters. We can compare Figure 4.1 with the results presented in Fig. 1(a) of Ref. [13] with the same field parameters and a perfect match is observed. In Ref. [13], an electric field $F(t)$ with a sine-squared envelope was used, whereas in the present work the vector potential $A(t)$ has a sine-squared envelope (2.7). The agreement between the results is expected, as the large N_c value makes the carrier envelope phase difference between the pulses insignificant. In Ref. [13], using the strong field approximation, it was shown that the probability distributions in the JES should be located at the energy conservation lines satisfying $E_N + E_e = E_0 + n\omega - U_p$, with the ground state energy $E_0 = -0.597$ a.u. and the ponderomotive energy $U_p = A_0^2/4 = 0.0483$ a.u. In

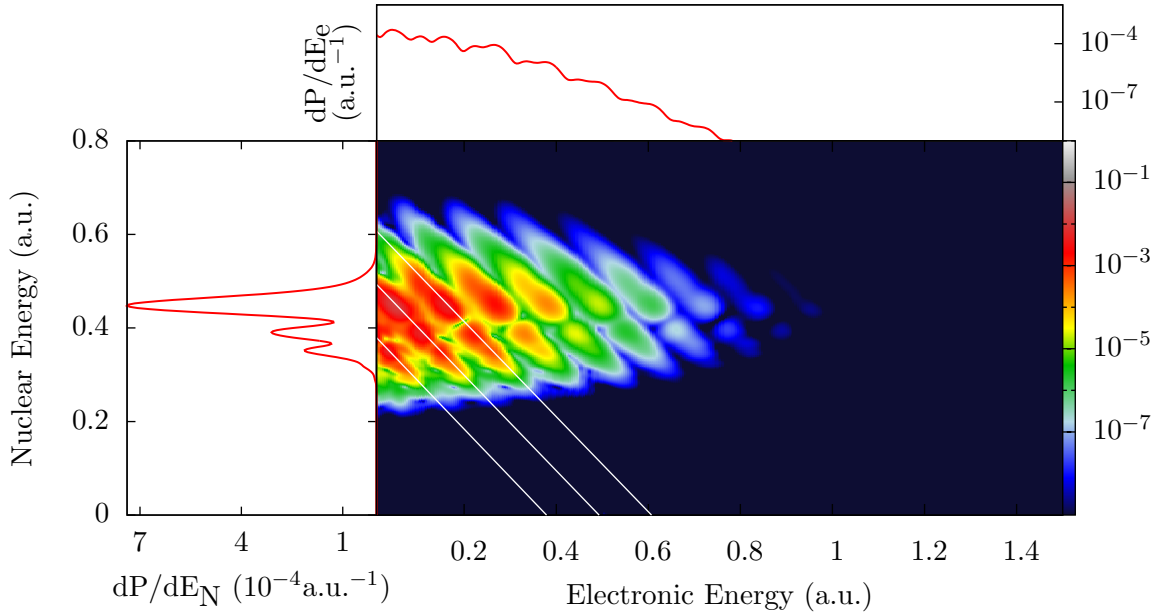


Figure 4.1: JES for DI [Eq. (3.26)] for a pulse with parameters $\lambda = 400$ nm, $N_c = 10$, and $I = 8.8 \times 10^{13}$ W/cm². The top and left side panels are the ATI and nuclear KER spectra, respectively. The diagonal (white) lines are energy conservation lines corresponding to n -photon absorption and satisfying $E_N + E_e = E_0 + n\omega - U_p$, with the leftmost line corresponding to $n = 9$.

Fig. 4.1 these energy conservation lines are clearly seen.

Figure 4.2(a) shows the nuclear KER spectrum for the 400 nm pulse with dissociation via the two first electronic states $\phi_{\text{el},0}^{g/u}$ corresponding to the $1s\sigma_g$ and $2p\sigma_u$ states. A comparison of the magnitudes of the probabilities with Fig. 4.1 shows that dissociation dominates over the DI process for these field parameters, although the DI yield cannot be entirely neglected as done in the N -surface model. The vertical dashed lines in Fig. 4.2(a) are the n -photon energy conservation lines satisfying $E_0 + n\omega = E_{\text{el},0}(R = \infty) + E_N$, where $E_{\text{el},0}(R = \infty)$ is the ground state energy of the hydrogen atom. Dissociation via $1s\sigma_g$ is located around the 2-photon line, while dissociation via $2p\sigma_u$ is located around the 3-photon line. This result can be understood by drawing the diabatic Floquet potential curves [26, 31], shown in Fig. 4.3(a). Starting from the vibrational ground state, the laser can induce a dissociative wave packet by the ATD process, which will move down the $2p\sigma_u - 3\omega$ curve. The time for the wave packet to move from the intersection between $1s\sigma_g - 0\omega$ and $2p\sigma_u - 3\omega$ at $R = 2.23$ a.u. to the intersection between $1s\sigma_g - 2\omega$ and $2p\sigma_u - 3\omega$ at $R = 4.7$ a.u. is approximately 204 a.u. (4.93 fs). At the latter intersection, part of the population can be transferred to the $1s\sigma_g - 2\omega$ curve by stimulated photoemission. The time for the population to move from $R = 4.7$ to $R = 10$ via the surface $1s\sigma_g - 2\omega$ is approximately 311 a.u. (7.52 fs), so the total time to reach $R = 10$ a.u. from the vibrational groundstate via the described pathway approximately equals the pulse duration. The pulse duration is therefore not long enough to induce transitions between the $1s\sigma_g - 2\omega$ and $2p\sigma_u - 1\omega$ curves, nor is it intense enough to lower the adiabatic Floquet potentials (gap proportional to electric field) to induce tunneling from the vibrational ground state ($v = 0$) to the $2p\sigma_u - 1\omega$ curve. This is the reason for

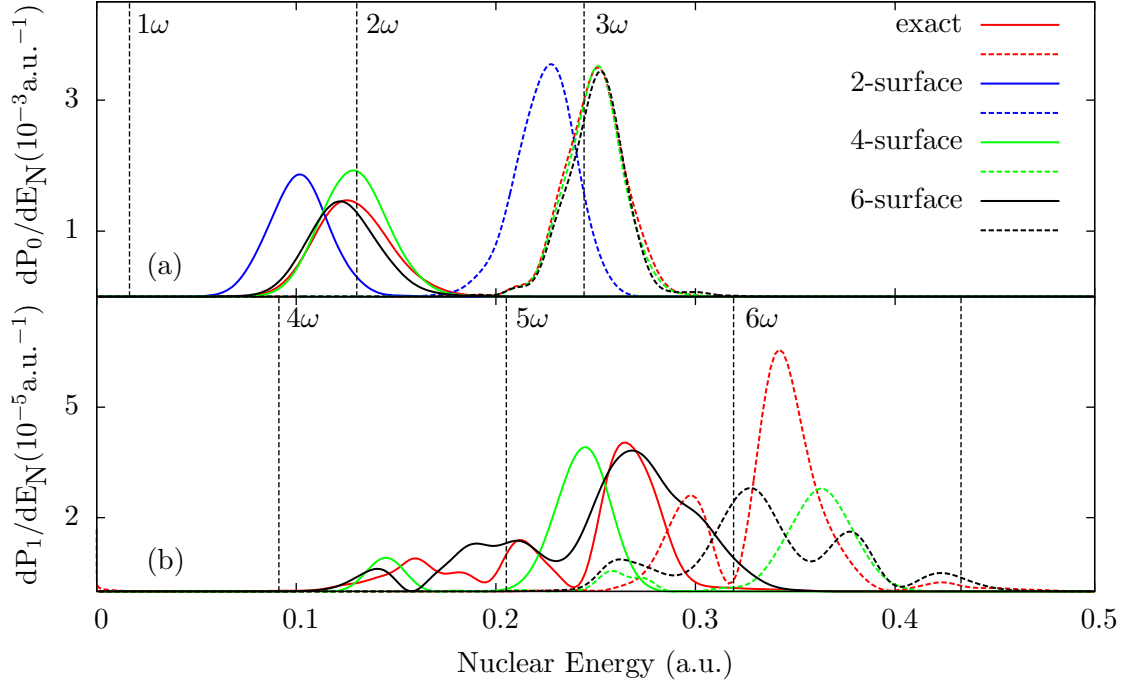


Figure 4.2: Dissociation spectra [Eq. (3.48)] for a pulse with $\lambda = 400$ nm, $N_c = 10$, and $I = 8.8 \times 10^{13}$ W/cm² with dissociation via (a) the first pair of gerade or ungerade states ($1s\sigma_g$ and $2p\sigma_u$), and (b) the second pair of gerade or ungerade states ($2s\sigma_g$ and $3p\sigma_u$). As indicated, different colors correspond to different methods used for the calculations. The solid and dashed lines show dissociation via the gerade and ungerade states, respectively. In the BO calculations, the spectra are scaled for easier comparison with the TDSE calculation. The vertical lines labeled by $n\omega$ ($n = 1, 2, \dots, 6$) denote photon absorptions above threshold (see text).

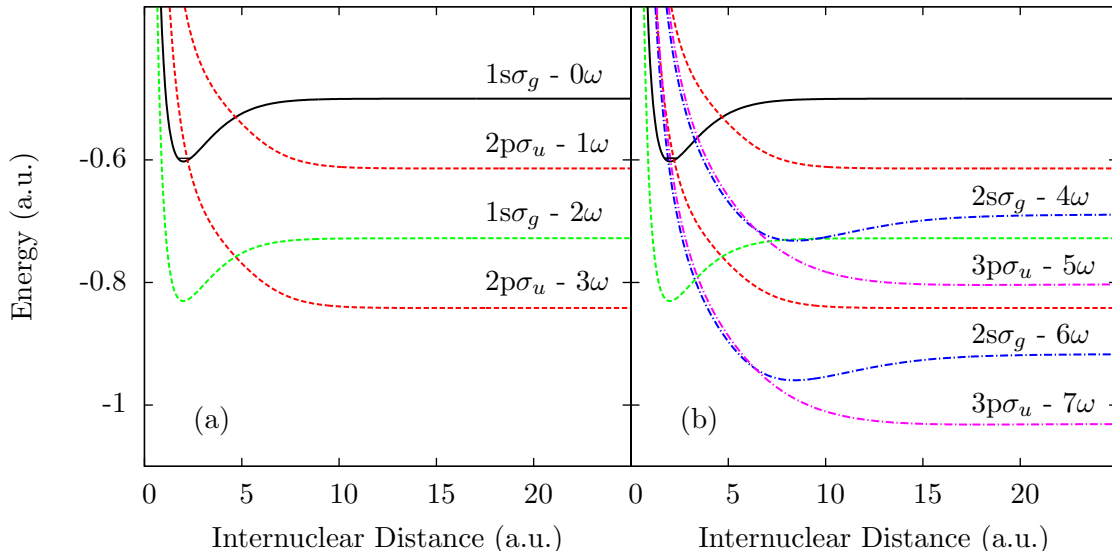


Figure 4.3: The diabatic Floquet potentials for the 1D H_2^+ model with $\lambda = 400$ nm. (a) Relevant dressed curves of $1s\sigma_g$ and $2p\sigma_u$ symmetry. (b) Additional dressed curves of $2s\sigma_g$ and $3p\sigma_u$ symmetry.

the absence of the 1-photon peak in the nuclear KER spectrum.

In addition to the TDSE calculation, calculations in the BO-approximation is performed for the N -surface model described in Sec. 2.3, with $N = 2, 4, 6$. In Fig. 4.2(a) it is seen that the nuclear KER yield for the 2-surface model is shifted more from the energy conservation lines than the TDSE calculation, indicating that the AC-Stark shift is inaccurately accounted for in the 2-surface model. Moreover, the ratio of the $1s\sigma_g$ dissociation yield to the $2p\sigma_u$ dissociation yield is overestimated in the 2-surface model. As seen in Fig. 4.2(a), the dissociation spectra is somewhat improved in the 4-surface model, where the peaks now are located at the correct positions, but the ratio of the $1s\sigma_g$ dissociation yield to the $2p\sigma_u$ dissociation yield is still overestimated. For the 6-surface model, the spectra almost overlaps with the spectra in the full TDSE calculation, with correct locations and ratio. This result indicates that when six BO states are used instead of four, additional dressed states can couple to $1s\sigma_g$, leading to depletion in the dissociation wave packet in $1s\sigma_g$, resulting in the correct spectra.

Figure 4.2(b) shows the nuclear KER spectrum for the 400 nm pulse with dissociation via the third and fourth electronic states $\phi_{el,1}^{g/u}$ corresponding to the $2s\sigma_g$ and $3p\sigma_u$ states. The vertical dashed lines in Fig. 4.2(b) are the n -photon energy conservation lines satisfying $E_0 + n\omega = E_{el,1}(R = \infty) + E_N$, where $E_{el,1}(R = \infty)$ is the energy of the first excited state in hydrogen. Dissociation via $2s\sigma_g$ is located between the 4- and 6-photon lines, while dissociation via $3p\sigma_u$ is located between the 5- and 7-photon lines.

To understand the dissociation spectrum in Fig. 4.2(b), the Floquet potential curves for $2s\sigma_g$ and $3p\sigma_u$ dressed by four to seven photons are plotted in Fig. 4.3(b). Furthermore, a study is performed where we gradually increase the intensity of the laser field and observe the resulting nuclear KER spectra, shown in Fig. 4.4. At lower intensities, $I \lesssim 2 \times 10^{13}$ W/cm² in Figs. 4.4(a) and 4.4(b), the 4-photon peak for the gerade state and the 5-photon peak for the ungerade state are clearly seen, stemming from the wave packet following the pathway $1s\sigma_g - 0\omega \rightarrow 2p\sigma_u - 3\omega \rightarrow 1\sigma_g - 2\omega \rightarrow 2\sigma_g - 4\omega$ and $3p\sigma_u - 5\omega$, shown in Fig. 4.3(b). This is also indicated by the $2s\sigma_g - 4\omega$ and $3p\sigma_u - 5\omega$ curves in Fig. 4.3(b). In Fig. 4.4(b) a small peak at around $E_N = 0.4$ a.u. is seen for the ungerade state and a smaller peak at around $E_N = 0.27$ a.u. is seen for the gerade state. These are the AC-Stark shifted 7-photon and 6-photon absorption peaks, respectively. Figure 4.3(b) clearly shows that the $3p\sigma_u - 7\omega$ and $2s\sigma_g - 6\omega$ curves cross the $1s\sigma_g - 0\omega$ curve at $R = 2$ a.u., below the energy of the vibrational groundstate ($v = 0$), leading to ATD processes explaining the peaks in Fig. 4.4(b). As the intensity is increased from Fig. 4.4(c) to Fig. 4.4(h), the 7-photon and 8-photon peaks are Stark shifted to lower nuclear energies, and additional structures in the peaks emerge. The additional structures are believed to be due to the interferences from the near-degeneracy of the $3p\sigma_u - 7\omega$ and $2s\sigma_g - 6\omega$ curves in Fig. 4.3(b) for $R < 7$ a.u., i.e. the strong coupling inducing many 1-photon absorption/emission paths that all lead to the same final dissociating state.

In Figure 4.2(b) the corresponding N -surface calculations with $N = 4, 6$ are shown. For the N -surface calculations, the peaks are located in the same energy region as the TDSE calculation, ranging from $E_N = 0.1$ to $E_N = 0.35$ for the $2s\sigma_g$ yields and from $E_N = 0.22$ to $E_N = 0.5$ for the $3p\sigma_u$ yields. However, the structures in the spectra are very different, indicating that coupling to even higher excited electronic states and the double continuum are important. Thus, the numerous previous descriptions of the dissociation process of H_2^+ where the 2-surface model has been used [3, 26, 32, 33, 34, 35, 36], are inadequate to describe all the correct dissociation processes.

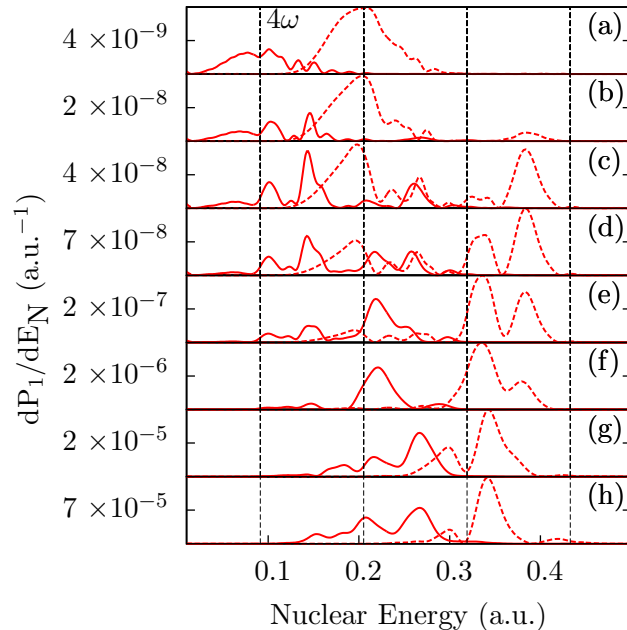


Figure 4.4: Each subplot is as in Fig. 4.2(b), now for the intensities: (a) $I = 1 \times 10^{13}$ W/cm², (b) $I = 2 \times 10^{13}$ W/cm², (c) $I = 3 \times 10^{13}$ W/cm², (d) $I = 3.5 \times 10^{13}$ W/cm², (e) $I = 4 \times 10^{13}$ W/cm², (f) $I = 5 \times 10^{13}$ W/cm², (g) $I = 8 \times 10^{13}$ W/cm², and (h) $I = 1 \times 10^{14}$ W/cm².

We have thus demonstrated that the t-SURFF method can be used to extract observables in dissociation and DI processes of H₂⁺. As a final remark, the size of the simulation volume used should be compared with the sizes of the volumes used by other methods. Two other methods have been used to determine the JES based on wave packet propagation. In one work [13], a projection on approximate scattering states was performed and a grid with $|x| \leq 1500$ was used for the electronic coordinate. In another work [30], a resolvent technique was used and a grid with $|x| \leq 3000$ was used for the electronic coordinate. Both these values significantly exceed the size of $|x| \leq 100$ used here.

4.2 Frequency dependence of JES

Now that the t-SURFF method is shown to work well for the extraction of spectra for DI and dissociation in H₂⁺, we will investigate the laser frequency dependence of the JES. Figure 4.5 shows the calculations for the laser parameters $N_c = 10$, $I = 8.8 \times 10^{13}$ W/cm² and $\lambda = 200\text{nm}, 400\text{nm}, 571\text{nm}, 800\text{nm}$. We will refer to the complete calculations, where we solve the TDSE including the nuclear and electronic motion, as the "full calculations". In the top panels of the subfigures, in addition to the ATI spectra of the full calculations, results for calculations with the nuclei clamped at the equilibrium distance are shown. We will refer to these calculations as the "clamped nuclei calculations". In the left panels of the subfigures, in addition to the KER for the full calculations, results for the reflection method calculations are shown. In the reflection method, the electron ionization is assumed to have occurred instantaneously, without having had time to interact with the nuclei. The remaining two protons will subsequently Coulomb explode, converting all its potential energy into kinetic energy. In a quantum picture, this corresponds to the

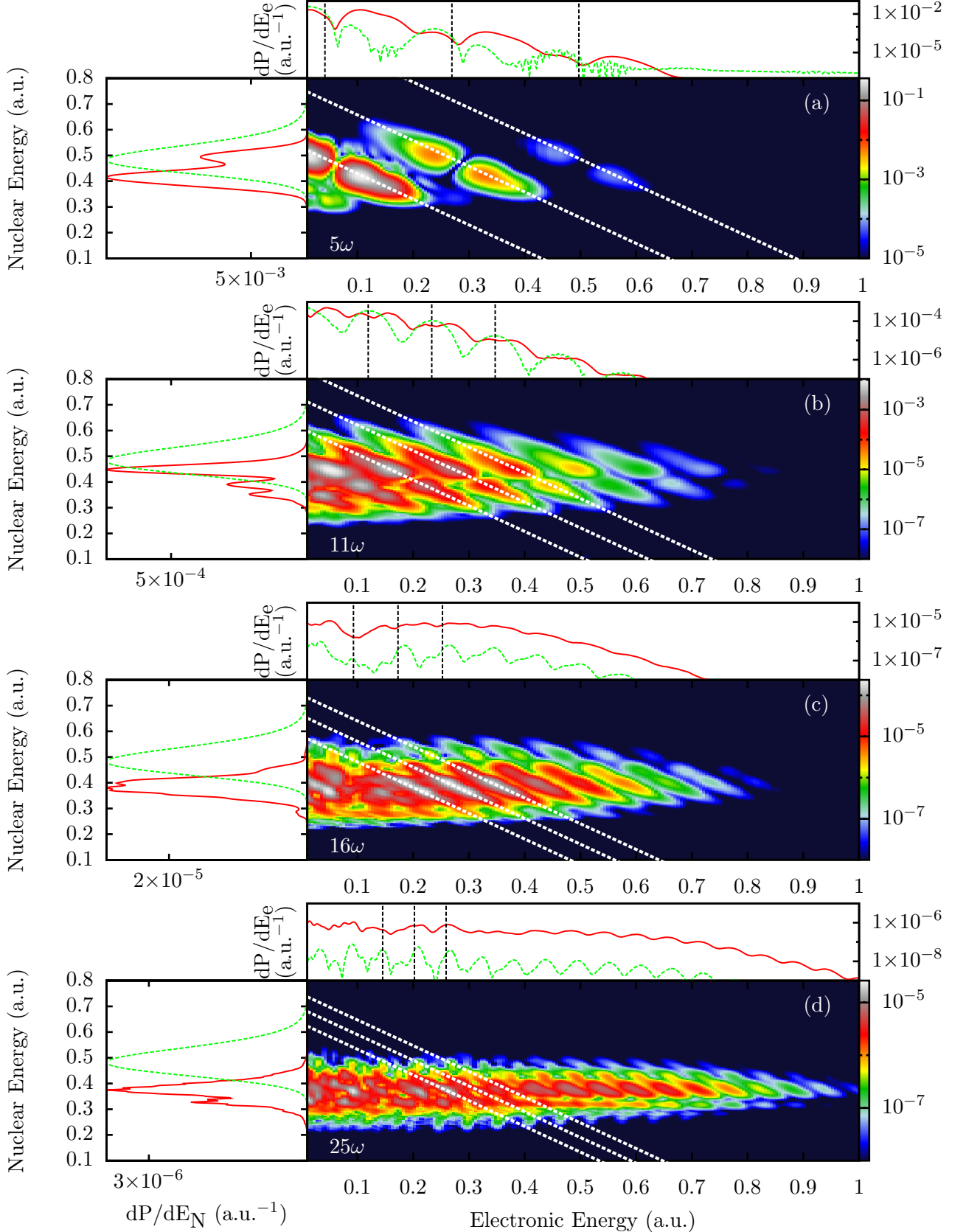


Figure 4.5: JES for DI [Eq. (3.26)] for laser pulses with parameters $N_c = 10$, and $I = 8.8 \times 10^{13} \text{ W/cm}^2$ and (a) $\lambda = 200 \text{ nm}$, (b) $\lambda = 400 \text{ nm}$, (c) $\lambda = 571 \text{ nm}$ and (d) $\lambda = 800 \text{ nm}$. The top and left side panels are the ATI and nuclear KER spectra, respectively. The diagonal (white) lines are energy conservation lines corresponding to n -photon absorption and satisfying $E_N + E_e = E_0 + n\omega - U_p$, with the leftmost line corresponding to the number in white. The dashed (green) lines in the ATI upper panels are calculations for the nuclei fixed at the equilibrium internuclear distance $R = 2.07$ and the dashed (green) lines in the KER side panels are calculations using the reflection method (scaled for comparison).

sudden approximation, with the probability of observing a nuclei energy E_N given by

$$\frac{\partial P}{\partial E_N} = |\langle \phi_{c,E_N} | \chi_\nu \rangle|^2, \quad (4.1)$$

where $|\phi_{c,E_N}\rangle$ is the Coulomb wave obtained as the solution to the TISE involving the bare nuclei Hamiltonian $T_N + V_N$ and χ_ν is the initial vibrational state which in this case is the ground state $\nu = 0$.

The reflection method predicts a single large peak at $E_N = 0.48$, corresponding to the internuclear distance $R = 2.07$ at which $|\chi_\nu(R)|^2$ is maximal. As seen in the left panels Fig. 4.5, this prediction is wrong for all the wave lengths considered. Indeed, the reflection principle is expected to work well only for very short pulses with pulse durations T_{pulse} much shorter than the characteristic timescale of the nuclear motion. In present calculations the pulse durations are 6.7 fs - 26.7 fs, comparable to the characteristic time scale of nuclear vibrations in $1s\sigma_g$ (15 fs), leading to the failure of the reflection method.

In the nuclear KER spectra of the full calculations shown in the left panels of Fig. 4.5, many structures are seen. Consider as an example the structures in the KER spectrum of Fig. 4.5(b). There are 3 peaks, one large peak located at $E_N = 0.449$ and two smaller peaks at $E_N = 0.352$ and $E_N = 0.390$. The large peak can be attributed to the enhanced ionization via the the 3-photon resonance between $1s\sigma_g$ and $2p\sigma_u$. This is seen in Fig. 4.6 as the crossing between the horizontal line indicating the location of the ground state vibrational energy and the $2p\sigma_u - 3\omega$ curves, located at $R = 2.19$, corresponding to a KER nuclear energy of $E_N = 0.457$. The peak at $E_N = 0.390$ can be interpreted as the enhanced ionization via the 7-photon resonance between $1s\sigma_g$ and $4p\sigma_u$, seen in Fig. 4.6 as the crossing between the horizontal line and the $4p\sigma_u - 7\omega$ curves, located at around $R = 2.83$, corresponding to a KER energy of $E_N = 0.353$. The peak at $E_N = 0.390$ can be interpreted as the channel opening of the direct nine-photon absorption channel, seen in Fig. 4.6 as the crossing between the $1s\sigma_g - 0\omega$ and the $1/R - 9\omega + U_p$ curves, located at around $R = 2.64$, corresponding to a KER energy of $E_N = 0.379$. Some of the structures in the KER spectra for the other laser frequencies shown in Fig. 4.5 can be explained in a similar fashion.

In Fig. 4.5, the discrepancy between the ATI spectra of the full calculations and the ATI spectra for the clamped nuclei calculations is also evident. For example, in the upper panels of Fig. 4.5(b) for the 400 nm pulse, the clamped nuclei calculation clearly shows the multi-photon-peaks separated by the photon energy, whereas in the ATI spectrum of the full calculation the multi-photon-peaks are not as clear, with each multiphoton peak containing several side peaks. Without the JES, it is impossible to tell which peak corresponds to which photon absorption channel. For example, if only the comparison with the ATI of fixed nuclei calculation was available, the largest ATI peak of the full calculation at around $E_e = 0.044$ could be interpreted as either the ten- or eleven-photon absorption peak. The JES reveals that the largest ATI peak actually contains contributions from both the 9-photon and 10-photon absorption lines, and that the first side peak at $E_e = 0.10$ stems from a peak in the 10-photon absorption line. Furthermore, the fixed nuclei calculation predicts the channel opening of the ATI process to be at minimum 10 photons, while the JES clearly shows that 9-photon absorption is also possible.

In the upper panel of Fig. 4.5(a) for the 200 nm pulse the same effect is seen in the ATI, with large peaks having contributions from several photon absorption lines in the JES and emerging side peaks. The side peaks actually overlap with the positions of the

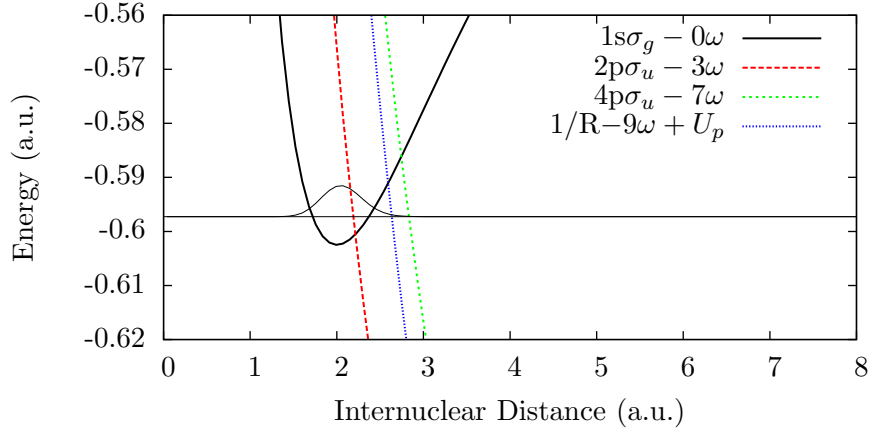


Figure 4.6: The electronic ground state $1s\sigma_g$ curve and dressed curves of $2p\sigma_u$ and $4p\sigma_u$ for a laser pulse with $\lambda = 400\text{nm}$. The (blue) dotted line shows $1/R - 9\omega + U_p$, and its crossing with the ground vibrational energy (horizontal line) indicates the internuclear distance for channel-opening for direct multi-photon ionization with 9 photons.

peaks of the clamped nuclei calculations, at the same energy positions and with almost the same amplitudes. These side peaks corresponds to contributions from ionization with nuclei being at the internuclear distance $R = 2.07$. The main peaks in the ATI are due to electron-nuclear correlation, indicating ionization from larger internuclear distances.

For the 571 nm calculations shown in Fig. 4.5(c), the Keldysh parameter is $\gamma = 2.36$, indicating that we are closer to the tunneling regime. For the part of the JES with $E_e \gtrsim 0.2$ a.u., the energy conservation lines are evident. At low electronic energies ($E_e \lesssim 0.2$ a.u.), the energy conservation lines are not as clear. Instead, interference patterns are seen, corresponding to different pathways leading to the same final double-continuum state. Similar blurring of the photon-absorption lines was reported in Ref. [30], where the change in the shape of the spectrum was interpreted as a signature of tunneling ionization. In the ATI spectrum of the full calculation, the multi-photon structure is not so obvious. The yield is also much higher in the full calculation compared to the fixed nuclei calculation. The pulse length is $T_{\text{pulse}} = 19$ fs, which means that a considerable part of the dissociative wave packet have reached a large internuclear distance where the ionization potential is smaller than at equilibrium, thus more ionization than the fixed-nuclei calculation is observed. For the 800 nm calculation in Fig. 4.5(d), the same effect is seen as in the case of Fig. 4.5(c), with blurred JES for low E_e and the clear energy conservation lines at high E_e .

All the above indicates that the JES spectra contains much more information than the pure ATI spectra. Analysing results from experiments where only the ATI spectra or the KER spectra are observed could lead to errors in the interpretation of the spectrum. Numerical calculations with fixed nuclei approximation, which has been extensively used in the litterature, will defer from the exact calculations involving nuclear motion.

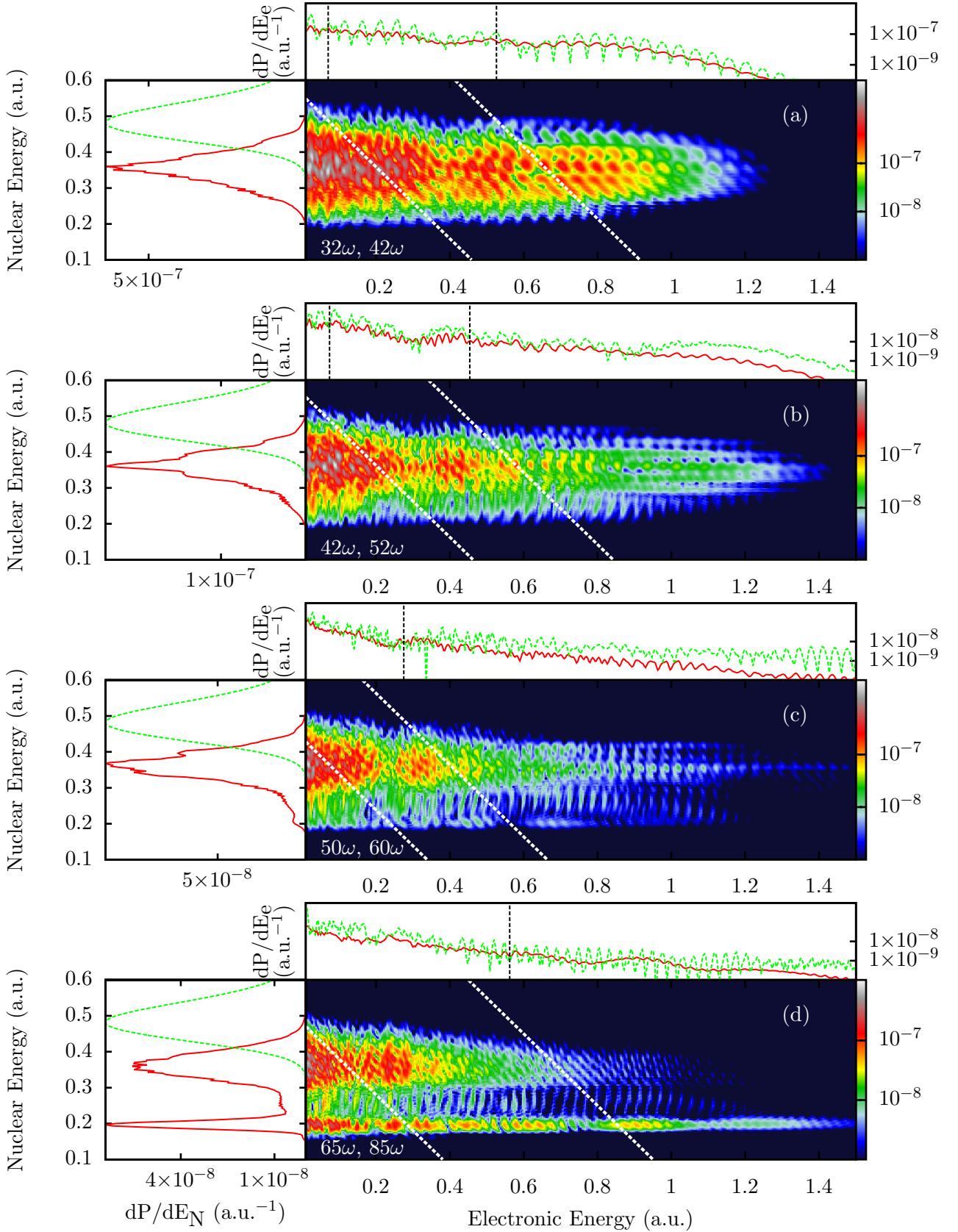


Figure 4.7: Same as Fig. 4.5, now with the pulse parameters $N_c = 10$, and $I = 8.8 \times 10^{13}$ W/cm² and (a) $\lambda = 1000$ nm, (b) $\lambda = 1200$ nm, (c) $\lambda = 1400$ nm and (d) $\lambda = 1600$ nm. Here, the KER spectrum obtained by reflection method and the ATI spectrum obtained by the fixed nuclei calculations are scaled for comparison.

4.3 Frequency dependence of JES - long wavelengths

The JES for DI using laser pulses with even longer wavelengths are also investigated, with the results shown in Fig. 4.7. For regions of the JES with high electronic energies, the diagonal multi-photon energy conservation lines satisfying $E_N + E_e = E_0 + n\omega - U_p$ are seen. Due to the small photon energies, the energy conservation lines are not as clearly separated as for the lower frequency cases shown in Fig. 4.5, which leads to neighbouring multi-photon lines overlapping. In Fig. 4.7(c), around $E_e = 0.8$, these overlaps result in almost vertical lines in the JES, which in the ATI spectrum in the upper panel of Fig. 4.7(c) leads to pronounced ATI spectra (compared to the ATI spectra in the upper panel of Fig. 4.7(b)). It should be emphasized that these vertical lines with constant E_e are not energy conservation lines, but the result of the overlapping of many multi-photon energy conservation lines.

For the $\lambda = 1600\text{nm}$ calculation, there is a high probability for the nuclei to have an KER of $E_N = 0.2$, seen as a clear horizontal line-structure in the JES of Fig. 4.7(d) and as a peak in the KER spectra of the left panel of Fig. 4.7(d). Inside this horizontal line-structure, the electronic energies are still separated by the photon energy. The horizontal structure is also discernible in the JES of Fig. 4.7(d) for the $\lambda = 1400\text{nm}$ calculation, but with a much smaller amplitude. The reason for this interesting structure is not yet clear at the moment and further investigation is needed. It could be due to some resonances at large internuclear distances, because for a shorter laser pulse with 5 cycles and the same wavelength $\lambda = 1600\text{nm}$, this horizontal structure is not seen in the JES (not drawn in this report).

4.4 Frequency dependence of JES - ultrashort pulse

A final study is performed to see how the energy is shared between the electron and the nuclei when H_2^+ is exposed to an ultrashort laser pulse. For a laser pulse with field parameters $I = 10^{13} \text{ W/cm}^2$, $N_c = 04$ and $\lambda = 28 \text{ nm}$, the photon energy is $\omega = 1.63$, the pulse bandwidth is $\omega_{\text{band}} \approx 1.6$ and the pulse duration is $T_{\text{pulse}} = 15.4$ (373 as). The photon energy is therefore much larger than the ionization potential at equilibrium internuclear distance $I_p(R_0) = 1.1$, indicating that one-photon transition to the double continuum is possible, with no intermediate resonances. Compared to the characteristic time of nuclear motion (15 fs), the pulse duration can be thought of as being instantaneous, with the nuclear degree of freedom frozen. We therefore expect the KER spectrum to be equal to the reflection method, with no additional structures. However, as shown in the left panel of Fig. 4.8(a), the reflection method and the full calculation yield quite different results. At $E_N = 0.51$ in the KER of the full calculation, a minimum is seen instead of a maximum in the reflection method. When the number of optical cycles of the laser pulse is increased, the minima in the KER and JES around $E_N = 0.51$ is still present, as seen in Figs. 4.8(b-d). The decrease of laser bandwidth from 1.63 for the 4 cycle pulse to 0.65 for the 10 cycle pulse is seen in Figs. 4.8(a-d) as the narrowing of probability around the energy conservation line for one-photon absorption satisfying $E_N + E_e = E_0 + \omega - U_p$. The minima in the KER and JES at around $E_N = 0.51$ is not understood and further investigation is needed.

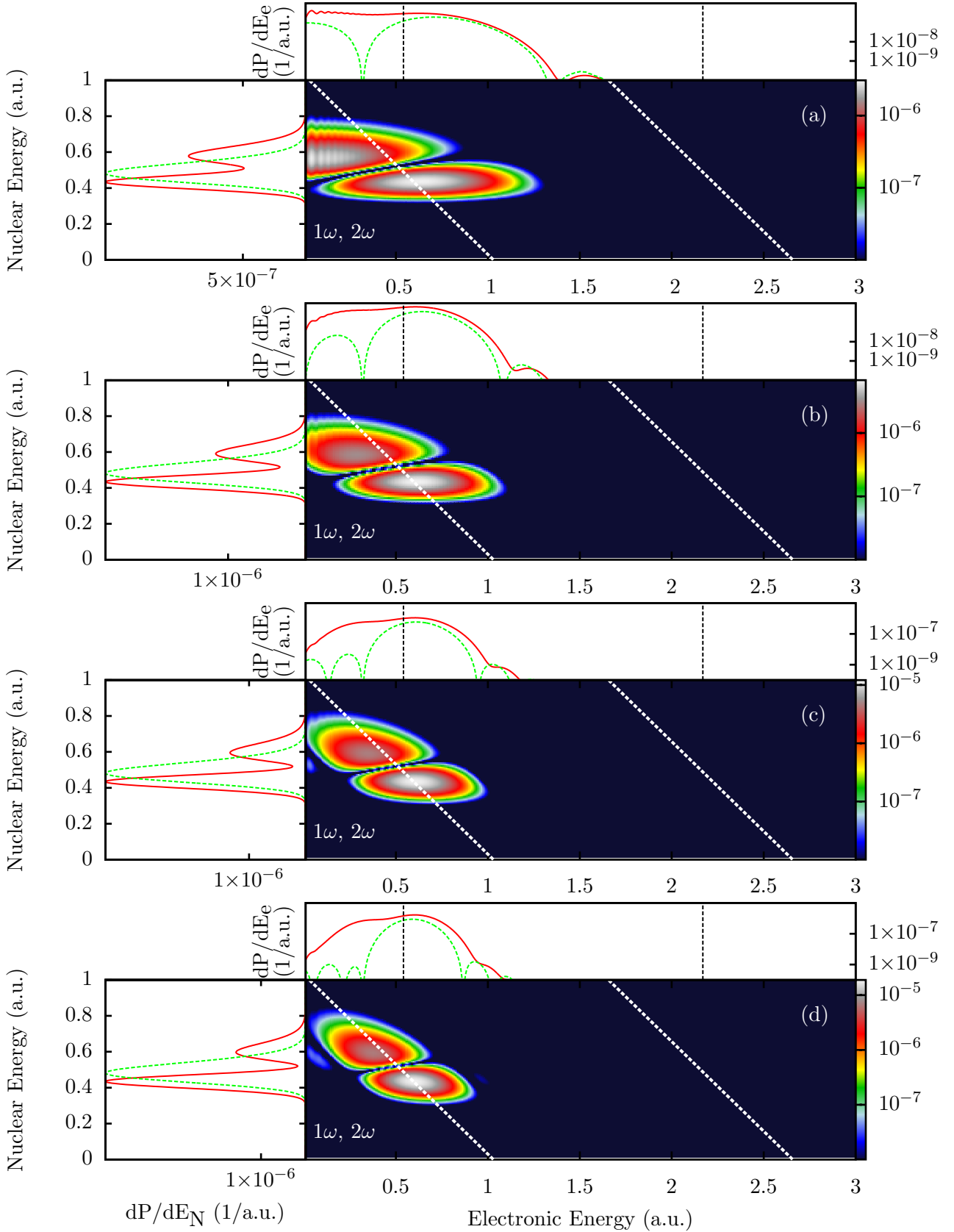


Figure 4.8: Same as Fig. 4.5, now with the pulse parameters $I = 10^{13}$ W/cm², $\lambda = 28$ nm, and (a) $N_c = 4$, (b) $N_c = 6$, (c) $N_c = 8$ and (d) $N_c = 10$. Here, only the KER spectrum obtained by reflection method is scaled for comparison, while the ATI spectrum obtained by the fixed nuclei calculations is not scaled.

Chapter 5

Conclusion

In this report we studied the dissociation and dissociative ionization of a model colinear H_2^+ molecule exposed to intense laser pulses. This was done by solving the TDSE in a coordinate grid, using CAPs as absorbers at the grid boundaries to reduce the simulation volume. The t-SURFF method [21, 22], which was introduced to extract fully differential ionization spectra of one and two-electron atomic systems, was extended to treat the molecule H_2^+ . Using t-SURFF, it was shown that complete differential spectra could be obtained for the continuum wave packets, including the channel-specific KER for dissociation and JES for dissociative ionization.

For the description of the dissociation process of H_2^+ , the 2-surface model in the BO-approximation, where only the two lowest bound electronic states were taken into account, was shown to be inadequate. The inclusion of six bound electronic states improved the resulting KER spectra in the $1s\sigma_g$ and $2p\sigma_u$ channels, but were still inadequate to describe KER spectra in $2s\sigma_g$ and $3p\sigma_u$. Thus, the higher excited bound electronic states and the double continuum are important for the dissociation processes.

For different pulse parameters in the multi-photon regime, it was shown for dissociative ionization that the ATI and the KER spectra were significantly different than the results obtained in the fixed nuclei approximation and in the reflection method, respectively. Side-peaks in the ATI spectra were seen to be due to contributions from different photon-absorption channels in the JES. The discrepancy of the the KER spectra in the TDSE calculation to the KER spectra in the reflection method were mostly due to enhancement of ionization by intermediate resonances. The ATI and KER spectra could only be quantitatively understood with the knowledge of the JES. For pulse parameters in the tunneling regime, the diagonal multi-photon absorption lines became less evident, with interference patterns emerging in the JES. A horizontal line structure in the JES located at low nuclear kinetic energies emerged for the longest wavelengths (1400nm-1600nm) considered. For ultrashort pulses with sub-femtosecond durations and photon energies much larger than the ionization potential, multi-peak structures were seen in the JES and KER spectra. This is puzzling because the characteristic time for these pulses were much shorter than the characteristic time for nuclear motion, so the reflection method is expected to work well here, with no multi-peak structure in the KER.

5.1 Outlook

In the nearest future, we will conclude the study on the one-dimensional H_2^+ model.

Afterwards, we plan to perform calculations on multi-electron atoms and molecules interacting with laser fields in three dimensions. A member of the group, S. Bauch, has already made a code for the time-dependent restricted-active-space configuration-interaction (TD-RASCI) scheme for a multi-electron system [37].

Generally, the wavefunction for a M -electron system can be expanded in a basis of Slater determinants:

$$|\Psi(t)\rangle = \sum_{I \in \Omega} C_I(t) |\psi_{i_1} \psi_{i_2} \cdots \psi_{i_M}\rangle \quad (5.1)$$

where $I = (i_1, i_2, \dots, i_M) \in \Omega$ specifies the occupied single particle spin-orbitals ψ_k . Let the number of single-particle spin-orbitals be $2M_b$ and let $\mathcal{B} = \{|\psi_1\rangle, \dots, |\psi_{2M_b}\rangle\}$ denote the single-particle basis. If $\Omega_{\text{FCI}} = \{i_1, \dots, i_M | 1 \leq i_1 < \dots < i_M \leq 2M_b\}$, then (5.1) is the full configuration interaction (FCI) expansion. The number of determinants in the FCI, $\binom{2M_b}{M}$, can be a huge number and therefore computationally demanding.

In the TD-RASCI method, the single-particle basis is divided into an arbitrary number P of partitions $\mathcal{B} = \mathcal{B}_1 \cup \dots \cup \mathcal{B}_P$. In each partition \mathcal{B}_i , restrictions on the allowed particle number is imposed. For example, to simulate the single ionization of a M -electron system, \mathcal{B} is divided into two partitions: one partition $\mathcal{B}_{\text{bound}}$ to describe the bound localized part of the wave packet, allowing M or $M-1$ electrons; and another partition $\mathcal{B}_{\text{cont}}$ to describe the continuum, allowing 0 or 1 electrons. In this way the number of terms in (5.1) and thereby the computational effort can be significantly reduced.

To obtain the single ionization momentum spectra, one could make use of diagonal elements of the one-particle reduced density matrix (RDM)

$$D(\vec{p}, t) = \sum_{pq} D_{pq}(t) \psi_p^*(\vec{p}) \psi_q(\vec{p}), \quad (5.2)$$

with the spin-independent orbitals in the momentum representation given by $\psi_q(\vec{p}) = \langle \vec{p} | \psi_q \rangle$, and

$$D_{pq}(t) = \sum_{\sigma} \langle \Psi(t) | \hat{c}_{p\sigma}^{\dagger} \hat{c}_{q\sigma} | \Psi(t) \rangle, \quad (5.3)$$

where σ is the spin label, p and q are the spatial orbital labels, and $\hat{c}_{p\sigma}^{\dagger}$ and $\hat{c}_{p\sigma}$ are respectively the creation and annihilation orbitals for the spin orbitals $|\psi_{p\sigma}\rangle$. The single ionization momentum spectra can be taken as $D(\vec{p}, T)$, where T is a sufficient large time after the end of the pulse. This scheme requires the knowledge of the wave function at large distances, and thus a large simulation volume is required. We plan to develop a method similar to the t-SURFF method, i.e. a method that is capable of obtaining single ionization spectra using a minimal simulation volume.

As described in the The t-SURFF method requires an efficient absorber for the absorption of the outgoing flux in the numerical calculations. Up until now, we have used CAPs, which always will cause reflections, the amplitude depending on the physical system and the pulse parameters used. In [38], infinite range exterior complex scaling (irECS) was introduced and demonstrated to be a perfect absorber for strong infrared fields. Implementation of irECS would also be a future task.

Bibliography

- [1] L. Yue and L. B. Madsen, *Phys. Rev. A* 88, 063420, 2013.
- [2] P. Agostini, F. Fabre, G. Mainfray, G. Petite, and N. K. Rahman, *Phys. Rev. Lett.* 42, 1127, 1979.
- [3] G. Jolicard and O. Atabek, *Phys. Rev. A* 46, 5845, 1992.
- [4] A. Giusti-Suzor, X. He, O. Atabek, and F. H. Mies, *Phys. Rev. Lett.* 64, 515, 1990.
- [5] B. D. Esry, A. M. Sayler, P. Q. Wang, K. D. Carnes, and I. Ben-Itzhak, *Phys. Rev. Lett.* 97, 013003, 2006.
- [6] M. Lewenstein, P. Balcou, M. Y. Ivanov, A. L’Huillier, and P. B. Corkum, *Phys. Rev. A* 49, 2117, 1994.
- [7] F. Krausz and M. Ivanov, *Rev. Mod. Phys.* 81, 163, 2009.
- [8] R. Kienberger, M. Hentschel, M. Uiberacker, Ch Spielmann, M. Kitzler, A. Scrinzi, M. Wieland, Th Westerwalbesloh, U. Kleineberg, U. Heinzmann, M. Drescher, and F. Krausz, *Science* 297, 1144, 2002.
- [9] J. Itatani, F. Quéré, G. L. Yudin, M. Y. Ivanov, F. Krausz, and P. B. Corkum, *Phys. Rev. Lett.* 88, 173903, 2002.
- [10] M. Schultze, M. Fieß, N. Karpowicz, J. Gagnon, M. Korbman, M. Hofstetter, S. Neppl, A. L. Cavalieri, Y. Komninos, T. Mercouris, C. A. Nicolaides, R. Pazourek, S. Nagele, J. Feist, J. Burgdörfer, A. M. Azzeer, R. Ernstorfer, R. Kienberger, U. Kleineberg, E. Goulielmakis, F. Krausz, and V. S. Yakovlev, *Science* 328, 1658, 2010.
- [11] T. Remetter, P. Johnsson, J. Mauritsson, K. Varjú, Y. Ni, F. Lépine, E. Gustafsson, M. Kling, J. Khan, R. López-Martens, K. J. Schafer, M. J. J. Vrakking, and A. L’Huillier, *Nature Phys.* 2, 323, 2006.
- [12] K. Klünder, J. M. Dahlström, M. Gisselbrecht, T. Fordell, M. Swoboda, D. Guénot, P. Johnsson, J. Caillat, J. Mauritsson, A. Maquet, R. Taïeb, and A. L’Huillier, *Phys. Rev. Lett.* 106, 143002, 2011.
- [13] C. B. Madsen, F. Anis, L. B. Madsen, and B. D. Esry, *Phys. Rev. Lett.* 109, 163003, 2012.
- [14] A. González-Castrillo, A. Palacios, F. Catoire, H. Bachau, and F. Martín, *J. Phys. Chem. A* 116, 2704, 2012.
- [15] R. E. F. Silva, P. Rivière, and F. Martín, *Phys. Rev. A* 85, 063414, 2012.
- [16] J. Wu, M. Kunitski, M. Pitzer, F. Trinter, L. Ph. H. Schmidt, T. Jahnke, M. Magrakvelidze, C. B. Madsen, L. B. Madsen, U. Thumm, and R. Dörner, *Phys. Rev. Lett.* 111, 023002, 2013.

- [17] S. Laulan and H. Bachau, *Phys. Rev. A* 69, 033408, 2004.
- [18] J. Feist, S. Nagele, R. Pazourek, E. Persson, B. I. Schneider, L. A. Collins, and J. Burgdörfer, *Phys. Rev. A* 77, 043420, 2008.
- [19] L. B. Madsen, L. A. A. Nikolopoulos, T. K. Kjeldsen, and J. Fernández, *Phys. Rev. A* 76, 063407, 2007.
- [20] J. Fernández and L. B. Madsen, *J. Phys. B* 42, 085602, 2009.
- [21] L. Tao and A. Scrinzi, *New J. Phys.* 14, 013021, 2012.
- [22] A. Scrinzi, *New J. Phys.* 14, 085008, 2012.
- [23] K. C. Kulander, F. H. Mies, and K. J. Schafer, *Phys. Rev. A* 53, 2562, 1996.
- [24] G. L. Ver. Steeg, K. Bartschat, and I. Bray, *J. Phys. B* 36, 3325, 2003.
- [25] W. Qu, Z. Chen, Z. Xu, and C. H. Keitel, *Phys. Rev. A* 65, 013402, 2001.
- [26] A. Giusti-Suzor, F. H. Mies, L. F. DiMauro, E. Charron, and B. Yang, *J. Phys. B* 28, 309, 1995.
- [27] L. V. Keldysh, *Zh. Eksp. Teor. Fiz.* 47, 1945, 1964. [Sov. Phys. JETP 20, 1307 (1965)].
- [28] M. D. Feit, J. A. Fleck Jr., and A. Steiger, *J. Comput. Phys.* 47, 412, 1982. ISSN: 0021-9991.
- [29] J. G. Muga, J. P. Palao, B. Navarro, and I. L. Egusquiza, *Phys. Rep.* 395, 357, 2004. ISSN: 0370-1573.
- [30] R. E. F. Silva, F. Catoire, P. Rivière, H. Bachau, and F. Martín, *Phys. Rev. Lett.* 110, 113001, 2013.
- [31] J. H. Posthumus, *Rep. Prog. Phys.* 67, 623, 2004.
- [32] L. Y. Peng, I. D. Williams, and J. F. McCann, *J. Phys. B* 38, 1727, 2005.
- [33] H. A. Leth, L. B. Madsen, and K. Mølmer, *Phys. Rev. Lett.* 103, 183601, 2009.
- [34] U. Thumm, T. Niederhausen, and B. Feuerstein, *Phys. Rev. A* 77, 063401, 2008.
- [35] T. Niederhausen and U. Thumm, *Phys. Rev. A* 77, 013407, 2008.
- [36] T. Niederhausen, U. Thumm, and F. Martín, *J. Phys. B* 45, 105602, 2012.
- [37] D. Hochstuhl and M. Bonitz, *Phys. Rev. A* 86, 053424, 2012.
- [38] A. Scrinzi, *Phys. Rev. A* 81, 053845, 2010.